Development and Testing of an Aerial Radiation Detection System

Indrajeet Yadav, *Member, IEEE*, Herbert G. Tanner, *Senior Member, IEEE*

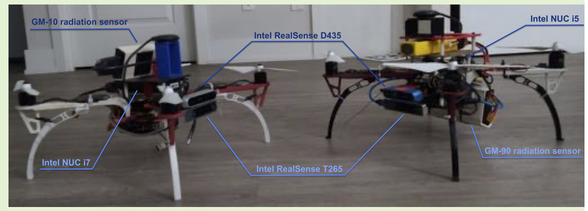

***Abstract*—This paper reports on the design and implementation of an airborne radiation detection system together with its associated signal processing and decision-making algorithms. This system is envisioned as the building block of an aerial radiation sensor network and it is specifically designed to detect weak radiological signatures in transit. The whole system is developed based on low-cost commercial off the shelf (COTS) components, and through a series of detailed experiments and Monte-Carlo tests, the paper shows how it can be deployed in time-critical application scenarios, where the time allocated to detect the source is limited. Performance metrics for the detection algorithms utilized in the system indicate that the reported technology can offer a significant improvement on the detection speeds compared to alternative techniques utilizing the same hardware resources.**

***Index Terms*—Mobility Enabled Aerial Radiation Detection, Radiation Sensor Calibration and Benchmarking.**

I. Introduction

REMOTE detection based on radiation counters is particularly challenging for at least two reasons. First, those counters pick up not only the source's radioactivity —assuming that one is present in their vicinity— but also ubiquitous, naturally occurring (background) radiation signals; from an inexpensive counter's (not spectrometer's) perspective, the two signals are of identical nature and indistinguishable once superimposed. The second reason relates to attenuation: although a kilogram of Highly Enriched Uranium (HEU) can emit as many as 4×10^7 gamma rays per second [2], shielding and attenuation over distance can limit the effective detection range to a few feet, and require detection times that can range from several minutes to hours. To put these in perspective, the gamma-ray emission of nuclear missiles containing HEU becomes comparable to background just 25 cm away from the warhead [18]. The problem is exacerbated by the motion of the signal source or the sensor. Not only does the mathematical model of the physical phenomenon change (becoming time-inhomogeneous), but now detectors have limited time to decide before the target disappears from sight: the sensors are faced with a problem of detecting in a matter of seconds, a weak time-varying signal, buried inside another signal of the same nature.

The measurement mechanism is mathematically modeled as a stochastic process, using the Poisson distribution to approximate the statistics of count arrivals at the sensor. Most advanced algorithms for the detection of nuclear material in motion expect to utilize a distributed network of *static* sensors. The data from the sensors are eventually fused, and based on the derived statistics different features of interest of the target in question can be estimated [8], [13], [14]. Due to the strong dependence of the Poisson process intensity on the distance between sensor and source (inverse square law [8]), one way to increase the signal-to-noise-ratio (SNR) is to exploit sensor mobility: move the sensors as close to the source as possible. Based on this idea, threat-based coverage over a given search area has been shown to increase by allowing limited sensor mobility [6]. Mobile sensors have also been steered through an information gain-driven search [4], [16], although such approaches work well mainly for high intensity radioactive sources.

Pahalajani et al. [9], [19] demonstrate that actively and dynamically steering mobile sensors for detecting weak (or heavily shielded) radiological material can result in significant improvement in detection performance. This is due to the fact that such motion control action allows them to rapidly close the distance to the source, boost their SNR, and thus acquire more informative data which eventually increases the accuracy of the decision-making. The aforementioned work focuses on developing the necessary signal processing theory, but stops short of demonstrating its benefits with some proof-of-concept experimental sensing testbed.

Different sensor mobility modalities can be utilized in such a framework; this paper focuses on aerial means of radiation measurement. Agility, affordability, and currently available onboard computation capability make modern multi-rotor unmanned aerial vehicles (UAVs) an attractive choice for

Manuscript first submitted on September 22, 2021. This work has been supported in part by DTRA under grant #HDTRA1-16-1-0039, and in part by ARL under #W911NF-20-2-0098.

Yadav and Tanner are with the Department of Mechanical Engineering at the University of Delaware, Newark, DE 19716 USA (e-mail: indragt@udel.edu, btanner@udel.edu).

Authors thank Michael Sebok from the Mechanical Engineering Department and William Fendt from the Environment Health and Safety group for their help in conducting the experiments.

such an application. There is some work and recent literature on UAV-based radiation detection for detecting radioisotopes. A California-based start-up [1], for example, introduced the Flycam-UAV which is a pilot (human)-operated drone that can detect alpha, beta and gamma particles along with some other chemical compounds. Alternatively, one can possibly mount on a UAV some low-cost radiation detector [3] or mapping [5] systems. Still, whether the focus is on sensor performance improvement, human operator deployment skill enhancement, or sensor motion strategy optimization, little attention is being paid to developing detection systems that can operate autonomously and can perform with minimal or no human intervention. Some work along this direction includes a real-time 3D gamma-ray and neutron mapping system that fuses the data from $Cs_2LiLa(Br,Cl)_6$:Ce (CLLBC) scintillators with a 3D Light Detection and Ranging (LiDAR) Sensor to localize gamma-ray/neutron source(s) in the presence of other heavy gamma sources [11]. A similar system focused on localization of sources from non-directional radiation detectors by integrating a multi-class object detection and 3D tracking with radiation detection models [7]. Essentially the idea was to fit/determine the time-dependent count rate that a detector is expected to encounter beforehand, and then track the objects over time and then based on the counts observed at the sensor. These approaches, however, deploy heavy and sophisticated sensors or detect high intensity sources (see Section VI for comparison).

Although simulation data have demonstrated the potential for performance increase [24], to this day there is little experimental evidence of competitive detection performance obtained with autonomous low-cost COTS aerial radiation sensor modules. This paper attempts to close this gap. In the case study considered, the objective is to steer DIY quadrotors fitted with inexpensive COTS radiation counters to determine in an expedited fashion whether or not a given moving target is radioactive. Specifically, the contributions of the work reported in this paper include:

- The detailed design and combined experimental/Monte-Carlo simulation-based approach to calibrate and benchmark a fully autonomous micro aerial vehicles (MAV) sensor system that facilitates the detection of mildly radioactive source of *known* intensity.
- The development of open-source ROS drivers for COTS Gieger-Muller (GM) counters along with their detailed calibration results; and
- Experimental application of efficient detection algorithms accompanied with results from field deployment.

II. Radiation Detection

Radiation sensor measurement is captured mathematically by a discrete random process, according to which when a gamma-ray (from the source or background) hits the sensitive area of the sensor, a "count" is recorded. In a probabilistic setup this is mathematically modeled as a time-inhomogeneous Poisson process [9], [19]. To set the stage for the description of this mathematical model, we need some preliminary constructs. To this end, imagine that on a measurable space $(\Omega, \mathscr{F})$, there is a counting process N_t, for $t \in [0, T]$, which represents the number of counts recorded at the sensor located at position $x \in \mathbb{R}^3$, up to (and including) time $t \in [0, T]$.

The decision-maker is faced with two competing hypotheses: H_0 expresses the opinion that the cumulative count rate can be attributed solely to naturally occurring background, and therefore the target of observation, located at a possibly time-varying position $x_t \in \mathbb{R}^3$, is benign; H_1, expresses the opinion that the cumulative rate should be attributed to the combined effect of background and the presence of a radiation source of intensity a counts per unit time on the target. The general (binary) hypothesis testing approach can be illustrated in Fig. 1. The leftmost (blue) bell curve indicates the Probability Density Function (PDF) under the hypothesis H_0 while the rightmost (red) bell curve indicates the PDF under hypothesis H_1. A judiciously selected value τ marks a decision threshold that strikes a balance between the risk of two decision errors: a false alarm (Type I error) with probability P_{FA} quantified by the area under the right tail of left curve on the right of the threshold, and a missed detection (Type II error) with probability P_{M} quantified by the area under the left tail of the right curve on the left of the threshold. In a Type I error, the test concludes that the data is consistent with the rightmost (red) curve (H_1) whereas in reality it is associated with the right tail of the leftmost (blue) curve (H_0). In a Type II error, the data is assumed to be coming from the leftmost (blue) curve (H_0) where in fact is coming from the rightmost (red) curve (H_1). With the possible exception where the curves represent normal distributions, analytical computation of these error probabilities is intractable.

What follows in this section is a description of an approach to bound the actual (intractable) probabilities P_{M} and P_{FA} using Chernoff bounds, which then become surrogates for the calculation of the optimal threshold. More details on these theoretical underpinnings can be found elsewhere [9].

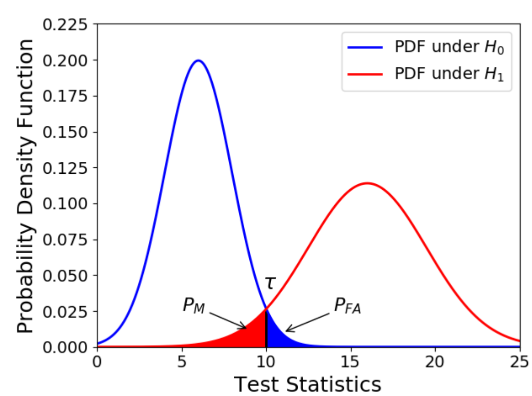

Fig. 1: The two competing hypotheses relative to the threshold picked for decision-making. The blue curve expresses H_0 while the red curve represents H_1. The filled blue area on the right side of the threshold τ illustrates the probability for a false alarm P_{FA} while the filled red area indicate the probability of miss P_M.

In essence, the two hypotheses H_0 and H_1 correspond, respectively, to two distinct probability measures $\mathbb{P}_0$ and $\mathbb{P}_1$

on $(\Omega, \mathscr{F})$. With respect to measure $\mathbb{P}_0$, the process N_t is a Poisson process with intensity $\beta(t)$ (this is the intensity of naturally occurring background radiation), while with respect to $\mathbb{P}_1$ the same process is Poisson with intensity $\beta(t)+\nu(t)$, where $\nu(t)$ is the intensity of the source as perceived by the sensor at time t. Functions $\beta(t)$ and $\nu(t)$ defined on $[0,T]$ are assumed to be bounded, continuous and strictly positive [9].

Function $\nu(t)$ captures implicitly the dependence of the sensor-perceived source intensity on the (time-varying) distance between the sensor and source. We utilize a functional representation of this dependence that is based on an inverse square law [8] relationship between range and perceived intensity. If χ denotes the sensor's cross-section coefficient, a denotes the source intensity, $x(t)$ and $x_t(t)$ are the (absolute) time-varying positions of the sensor and the target, the perceived intensity at the sensor can be expressed as

$$\nu(t) = \frac{\chi a}{2\chi + \|x(t) - x_t(t)\|^2} \ , \tag{1}$$

where the coefficient 2 in front of χ captures the fact that up to half of the effective surface of an omni-directional sensor can face a single source at any given time instance.

A test for choosing between H_0 and H_1 is considered an event B_1. The occurrence of event B_1 is ascertained on the basis of sensor observations over $[0,T]$, and has the following significance: for an outcome ω, if $\omega \in B_1$, decide H_1; otherwise, that is if $\omega \in B_0 \triangleq \Omega \setminus B_1$, decide H_0. For such a test, two types of errors can occur. A *false alarm* occurs if $\omega \in B_1$ with H_0 being the correct hypothesis; this occurs with probability $\mathbb{P}_0(B_1)$. A *missed detection* occurs with probability $\mathbb{P}_1(\Omega \setminus B_1)$, if $\omega \in B_0$ while H_1 is true. In this setting, the optimal test for deciding between H_0 and H_1 is a likelihood ratio test (LRT) obtained as follows [9]. Let τ_n for $n \geq 1$ denote the n^{th} jump time of N_t (when the sensor registers a count), and with the convention that $\prod_{n=1}^{0}(\cdot) = 1$, let the likelihood ratio L_T be [20]

$$L_T = \exp\left(-\int_0^T \nu(s)\,\mathrm{d}s\right)\prod_{n=1}^{N_t}\left(1+\frac{\nu(\tau_n)}{\beta(\tau_n)}\right) \ . \tag{2}$$

Assume that P_1 is absolutely continuous with P_0, and that H_0 and H_1 are equiprobable [17]. Then for a specific fixed *threshold* $\gamma > 0$, the test

$$L_T \underset{H_0}{\overset{H_1}{\gtrless}} \gamma \tag{3}$$

is optimal in the (Neyman-Pearson) sense, meaning that if A_2 is any other test whose probability of false alarm $P_0(A_2) \leq P_0(L_T \geq \gamma)$, then the probability of a miss(ed detection) for (3) is at least as low as that for A_2, i.e. $P_1(L_T < \gamma) \leq P_1(\Omega \setminus A_2)$. With $\mu(t) \triangleq 1 + \frac{\nu(t)}{\beta(t)}$, constants $p \in (0,1)$ and $\eta \triangleq \log\gamma$, and

$$\Lambda(p) \triangleq \int_0^T \left[\mu(s)^p - p\,\mu(s) + p - 1\right]\beta(s)\,\mathrm{d}s \ , \tag{4}$$

one can express Chernoff bounds on the probability of false alarm P_{FA} and missed detection P_{M} as [9]

$$P_{\mathsf{FA}} \leq \exp\left(\inf_{p>0}[\Lambda(p) - p\,\eta\,]\right)$$
$$P_{\mathsf{M}} \leq \exp\left(\inf_{p<1}[\Lambda(p) + (1-p)\eta]\right) \ .$$

If an upper limit $\alpha > 0$ is set on the bound on probability of false alarm, then there exists a unique solution $p^* \in [0,1]$ to $\exp\left(\inf_{p<1}[\Lambda(p) + (1-p)\eta]\right) = \alpha$ for which the tightest bound on the probability of missed detection is obtained, and the exponent in the bound on the probability of false alarm and missed detection, respectively, is [9]

$$\begin{aligned}\mathcal{E}_{\mathcal{FA}} &= \int_0^T [p^*\mu(s)^{p^*}\log\mu(s) - \mu(s)^{p^*} + 1]\beta(s)\,\mathrm{d}s \\ &= -\log\alpha \end{aligned} \tag{5}$$

$$\mathcal{E}_{\mathcal{M}} = \log\alpha + \Lambda^{'}(p^*) \ , \tag{6}$$

where the derivative $\Lambda'(p)$ is expressed as (cf. [20, §2.4])

$$\Lambda^{'}(p) = \int_0^T [\mu(s)^p\log\mu(s) - \mu(s) + 1]\beta(s)\,\mathrm{d}s \ . \tag{7}$$

Suppose that the distance between target and sensor, $\|x(t) - x_t(t)\|$, is regulated by a control input u; then ν, and consequently μ, depend implicitly on u. Based on this observation, an optimal control problem can be formulated as follows:

Find the u that optimizes $\Lambda^{'}(p^*)$ for a given upper limit α on the bound on the probability of false alarm.

Irrespective of whether $\|x(t) - x_t(t)\|$ is deterministic or stochastic, it can be shown that the optimal sensor management strategy u for sensors is to close the distance between source and sensor as quickly as possible [19], [22].

III. Aerial Sensor Design

The term Aerial Radiation Sensor is used for the custom-build MAVs fitted with GM counters (see Abstract graphical). The quadrotors are based on a DJI Flamewheel F450 frame. Computationally, one of them features an on board Intel NUC Core i7-8650U quad core CPU@1.9 GHz×4 while the other has an Intel NUC Core i5-7300U dual core CPU@2.6 GHz×2. Both uses 16GB RAM, 128GB SSD and a Pixhawk flight controller that is given the desired thrust magnitude and rate commands, which are then tracked using an onboard body rate controller. An Intel RealSense-D435 RGB-D camera (640×480 pixel, 30 Hz) provides pointcloud information as well as images for target detection, while the RealSense-T265 VI-sensor (2 848×800 pixel 30 Hz cameras with a 200 Hz IMU) is used for inertial odometry and local navigation. This lightweight sensor package provides reliable depth information for up to 5 m.

One of the quadrotors (left) is fitted with a GM-10 sensor while the other carries a GM-90 sensor. Both quadrotors utilize an open-source state estimation library called Open-VINS to get the real-time visual-inertial (VI) odometry at 30 Hz. Based on these estimates of vehicle state, a custom onboard nonlinear receding horizon flight controller performs point-to-point navigation or target interception and tracking [23]. The ROS drivers for the sensors can be found at `https://github.com/indsy123/Radiation_sensor_drivers`.

IV. Aerial Radiation Sensor Calibration

This section describes the calibration procedure for the two Gieger-Muller (GM) counters (GM-10 and GM-90 from Blackcat Systems).[1] The calibration procedure first verifies that the mathematical model for (1) accurately captures the the sensor-perceived source intensity. Once this is confirmed, the next step is the determination of the sensor cross-section parameter χ, followed by the estimation of the recommended sensor integration time for a source of particular intensity.

Explicit verification of (1) is warranted on the basis that the model has been derived considering the solid angle subtended by the sensor on to the source, without considering explicitly the *intrinsic efficiency* of the sensor. The intrinsic efficiency is the ratio of the number of particles detected by the sensor to the number of particles incident on it. In order to include this factor, it is anticipated that the first-principles model (1) may need modification.

A combination of 12 weak gamma sources (3 Cs-137 sources of $1\,\mu$Ci radioactivity, 3 Co-60 sources of $1\,\mu$Ci each, 4 Sr-90 sources of $0.1\,\mu$Ci each, and 2 Ra-226 sources of $0.9\,\mu$Ci) collectively giving around $8.2\,\mu$Ci were used for the bench-marking the sensors and during the testing. To determine the sensor cross-section coefficient χ and the intensity of the source a as they appear in (1), the counts obtained by the GM counters were recorded for a total of 200 seconds, keeping the radiation source at various fixed distances from the sensor.

Figure 2 shows the results of this experiment for the GM-10 counter. The dashed red curve shows the power function fit on the number of counts observed by the sensor due to its vicinity to the $8.2\,\mu$Ci source. The equation of this curve is $63.51 \times \|x(t) - x_t(t)\|^{-0.88}$. In order to account for the unknown intrinsic efficiency we replace the exponent of the squared distance in (1) with a parameter $\epsilon > 0$ to be experimentally determined:

$$\nu(t) = \frac{\chi a}{2\chi + \|x(t) - x_t(t)\|^{\epsilon}} \quad . \tag{8}$$

The value of exponent ϵ is now determined for each sensor experimentally. For the GM-10 counter, the value for this parameter that offers the best fit turn out to be $\epsilon = -0.88$. With this parameter, (8) matches reasonably the experimentally observations for the GM-10 counter marked by the dashed green curve in Fig.-2(a). Given ϵ, the values for χ and a are now determined as follows.

Notice that in (8), as $\|x(t) - x_t(t)\| \to 0$, $\nu \to a/2$. Parameter a is determined assuming that the source strength should be double the count rate when the source is incident to (touching) the sensor—the reasoning being that the sensor then captures half of the source's emissions. Since $1\,\mu$Ci = 37000 decays/second, the source strength is thus estimated at $a = 8.2 \cdot 37000 = 3.034 \times 10^5$ counts per second (CPS). With a fixed, χ can be determined using a set of n independent measurements as

$$\chi = \frac{\sum_{i=1}^{n} \|x - x_{t_i}\|^{\epsilon}}{a \sum_{i=1}^{n} \frac{1}{\nu_i} - 2n} \quad ,$$

a process that yields a value for χ equal to 1.22×10^{-6} m^2. The small value of χ is justified given that it also captures the (low) efficiency of the sensor. Background activity for the GM-10 counter is similarly estimated at 0.15 CPS.

Similar results for the GM-90 counter are shown in Fig. 2(b). The background count rate for this sensor is measured at 1.0 CPS and the sensor cross-section coefficient χ is estimated at 4.0×10^{-6} m^2. The power function fit (red line) for this sensor is expressed in the form $510.812 \times \|x(t) - x_t(t)\|^{-1.01}$ and for this sensor the best fit for the exponent of $\|x(t) - x_t(t)\|$ in (8) is found to be $\epsilon = 1.0$.

These plots also indicate that the radioactivity from this source blends completely into the background at about 2.5 m away from the source and therefore the sensors have to be within this range to the source to maintain a reasonable chance of successful detection within a fixed time window.

Reasonable values for this fixed time window T in (2) are set for each sensor through a process of Monte-Carlo simulations using GAZEBO. A simulated model of a quadrotor was used to intercept a moving target while maintaining a distance of 2.5 ± 0.25 m from it. The detection algorithm described in Section II is executed in each Monte-Carlo run. The detection test itself is a Neyman-Pearson fixed time interval binary hypothesis test (refer to [9] for a more detailed exposition). At the heart of the test is a likelihood ratio based on a statistic L_T (see (2)) calculated based on the history of relative distance between the airborne radiation sensor and the hypothesized source, in addition to the aggregated counts over the sensor's (predetermined) integration time interval T. This likelihood ratio is compared against a fixed threshold value γ that also depends on the relative distance and the acceptable bound on the probability of false alarm P_{FA}. The optimal value of p^* is obtained by solving (5) and then the threshold is calculated by evaluating (7) at p^*. The bound on probability of false alarm for these tests was set to 0.1.[2] The natural process of gamma emission is simulated using the thinning algorithm [10], using the calibration parameters for the sensors obtained above. With this setup, the output of the thinning algorithm in terms of counts generated matches the experimental observations with the combined source.

The scenario with GM-10 parameters was repeated a total of 100 times, 50 times each with and without the presence of the simulated source. The total run time was set to $T = 168$ seconds. Fig. 3(a) shows the likelihood ratio L_T and detection threshold γ on a log-log scale. Green dots correspond to the outcome of the LRT when the source was present and the red squares correspond to the decision made based on the test when there was no source. The straight line represents the threshold boundary separating a decision supporting H_0 ($L_T < \gamma$) from a decision supporting H_1 ($L_T > \gamma$). The simulated sensor failed to detect the source 5 times out of a total of 50, providing a Monte-Carlo estimate

[1] http://www.blackcatsystems.com/GM/products/GM10GeigerCounter.html

[2] This value may seem high at first glance, but one needs to take into account that in a Neyman-Pearson test the two competing hypotheses are supposed to be equiprobable. When in practice the prior probability of a target to be radioactive is much smaller than 0.5, the probability of false alarm adjusts accordingly.

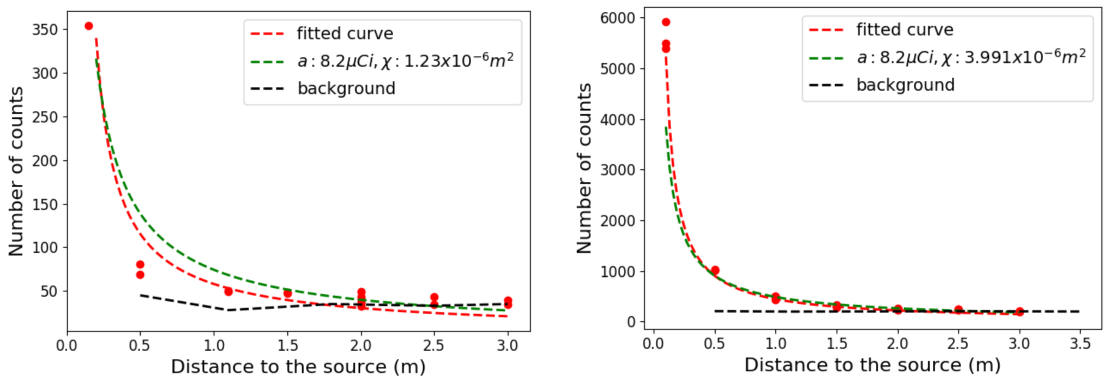

(a) GM-10 counter (b) GM-90 counter

Fig. 2: Variation of Number of Counts with the Distance. (a) Results for GM-10. Red dots show the counts observed at a specific distance from the source. Black dashed curve depicts the background. Dashed red curve is the fitted power curve while Green curve is obtained by determining the values of a and χ from the data and using equation (8).(b) Similar results for GM-90.

for the probability of missed detection at 0.1. Similarly, the simulated sensor triggered a false alarm (decided on the presence of a source where none was there) 3 out of 50 times, resulting in a Monte-Carlo estimate for the probability of false alarm of 0.06, below the acceptable bound.

Figure 3(b) shows the variation in the sensor integration window length, T, necessary to make a decision based on the LRT. The figure marks the mean value for T, along with its 5$^{\text{th}}$ and 95$^{\text{th}}$ percentiles. Note that that although the maximum T that any simulation run could use had been set at 168 seconds, since detection calculations were performed every second, it was possible to also ascertain a minimum T that would result in successful detection. The median of required detection interval comes out to be approximately 100 sec with 95 percentile being 135.4 sec. Based on these results it can be confidently concluded that given a detection interval of approximately 2.5–3 min, a gamma source of $8.2\,\mu$Ci strength can be accurately detected using the current setup with the probabilities of false alarm and missed detection being those shown in Fig. 3(a).

The same process was repeated using the estimated parameters for the GM-90 counter, using the same characteristics for source intensity and range to sensor. Given its increased sensitivity compared to the GM-10 counterpart, the GM-90 counter appeared to need approximately $T = 70.4$ seconds, with a 5% and 95% percentiles at 65.5 and 96 seconds, respectively. Figures 3(c) and 3(d) shows the Monte-Carlo simulation detection results for the GM-90 counter.

V. Field Deployment Results

The final sensor performance tests involve a sequence of controlled experiments in which the efficiency of both aerial radiation sensors, and the variation of their recorded count mean rate as a function of their distance to the source is estimated in field conditions, both outdoors as well as indoors (Fig. 4). The MAVs featured in the Abstract graphical were deployed in both indoor and outdoor experiments, where their task was to locate and intercept a ground target (the remotely controlled ClearPath Robotics Jackal) moving along an unspecified path with unknown but bounded speed. The ground robot carried an approximately 8.2 μCi radioactivity source which the MAVs had to detect.

The receding horizon planning and control strategy [23] running onboard the MAV ensures that it closes this distance to the target as fast as possible, thus enabling the onboard Geiger counters to collect informative measurements. The target detection is based on an SSD-Mobilnet V2 based neural network which was trained on over 500 images of the Jackal robot in different background and lightening conditions. The network utilizes a 300×300 fixed image resizer to increase the inference speed. Adam optimizer was used for a total 20000 steps. All other parameters are kept to their default values. The average 3D position of the inliers within the bounding box (obtained from the neural network) has been obtained utilizing the disparity image from the RGB-D sensor. This aggregate relative position measurement is used by a linear Kalman filter, which based on a constant-acceleration motion model for the target, returns 3D position estimates of the target with respect to the MAV's center of gravity (COG) and feeds it to the motion planning algorithm.

A. MAV with GM-10 Counter

The first set of experiments involved the MAV with GM-10 counter tracking the ground vehicle for certain time T. The MAV has to maintain a certain minimum distance from the target to keep it in its camera's limited FOV; as a result, the relative distance should not be reduced to arbitrarily small levels. Variations in the relative distance between sensor and source can be attributed to motion perturbations, as the (remotely operated) target performs avoidance maneuvers. Although generally robust, the neural network running on board the MAV does not furnish guarantees against false target identification, and this can contribute to relative distance estimate outliers (see Fig. 5, around the 85$^{\text{th}}$ second).

Figure 5 presents the results of one radiation detection experiment conducted in an indoor environment (an abandoned industrial warehouse, see Fig. 4) using the MAV that features the GM-10 counter. It shows the evolution of the estimate of the relative distance d between the MAV and the ground robot as the latter moves with unknown and time-varying speed. The relative distance is estimated in real

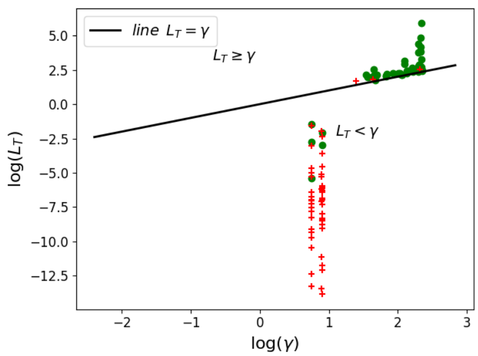

(a) Error Probability Bounds and T

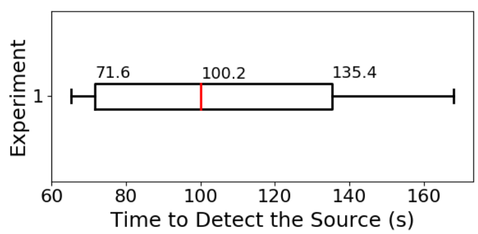

(b) Box Plot of Detection Interval T

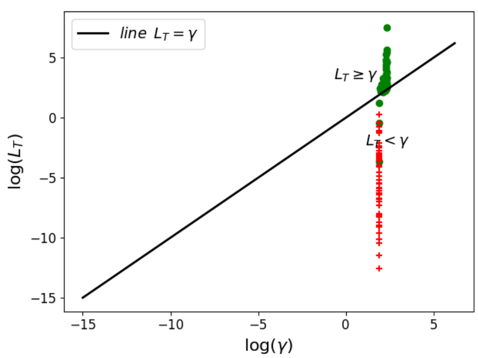

(c) Error Probability Bounds and T

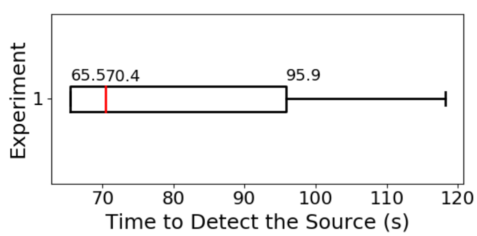

(d) Box Plot of Detection Interval T

Fig. 3: Monte-Carlo sensor-based decision-making simulations results. (a) Scatter Plot showing outcomes of an likelihood ratio test (LRT). The green dots • correspond to LRT performed in the presence of the source, while the red crosses + mark outcomes of the LRT when no source was present. The solid black line represents the threshold separating a decision supporting H_0 ($L_T < \gamma$) from a decision supporting H_1 ($L_T > \gamma$). (b) Box plot showing the variation of detection interval T required to successfully detect the source during Monte-Carlo simulations. (c) and (d) Similar results for GM-90 sensor.

time via the target tracking pipeline. The dashed curves in Fig. 5 indicate the evolution of Chernoff bounds on the probability of false alarm, P_{FA}, and probability of missed

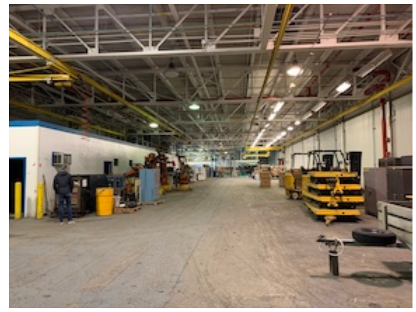

Fig. 4: Indoor facility where some of the autonomous sensor target interception and source detection experiments were conducted.

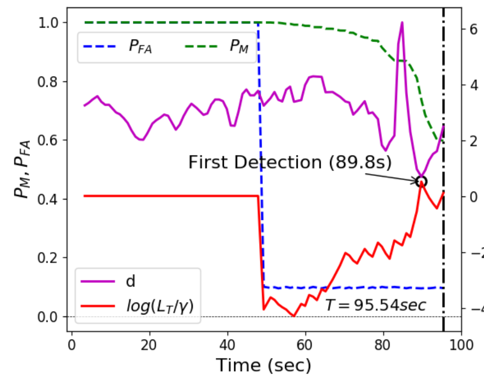

Fig. 5: Detection parameters for an autonomous airborne GM-10 sensor as a function of decision time T. Bound on probability of false alarm: dashed blue; bound on the probability of missed detection: dashed green; ratio $\log {}^{L_T}/_{\gamma}$: solid red; sensor-source distance: solid magenta.

detection P_{M} (see [9]). The bound on the probability of false alarm appears to drop below the acceptable upper limit after approximately 50 seconds from the start of the experimental run, after which the bound on the probability of missed detection P_{M} also starts to slowly decrease monotonically—the latter is a decreasing function of the sensor integration time and distance between sensor and source [9]. The graph of the logarithm of the likelihood ratio L_T over the detection threshold γ over time is marked in red; this process is stochastic because it depends directly on the arrival time of gamma rays on the sensor. The initial segment of the red curve corresponds to the initial time period during which the constraint on P_{FA} has not been satisfied and $\log {}^{L_T}/_{\gamma}$ has been kept at 0. The experiment is concluded at 95.54 seconds and the likelihood ratio L_T exceeds its threshold value at 89.8 seconds indicating the presence of the radiation source on the ground target (marked with a black circle in the plot). (The likelihood ratio had actually crossed the threshold before that time, but the experiment was continued because that event was observed significantly earlier than the recommended sensor integration window.)

B. MAV with GM-90 Counter

Figures 6(a) and 6(b) showcase two different runs where the MAV featuring the GM-90 counter was utilized. The experimental run of Fig. 6(a) shows an instance where the airborne sensor did not have enough time to detect the source. This experiment was performed in the same indoor facility as that used for the run of Fig. 5. Here, the radiation sensor integration window is 56 seconds. In this case, the bound on

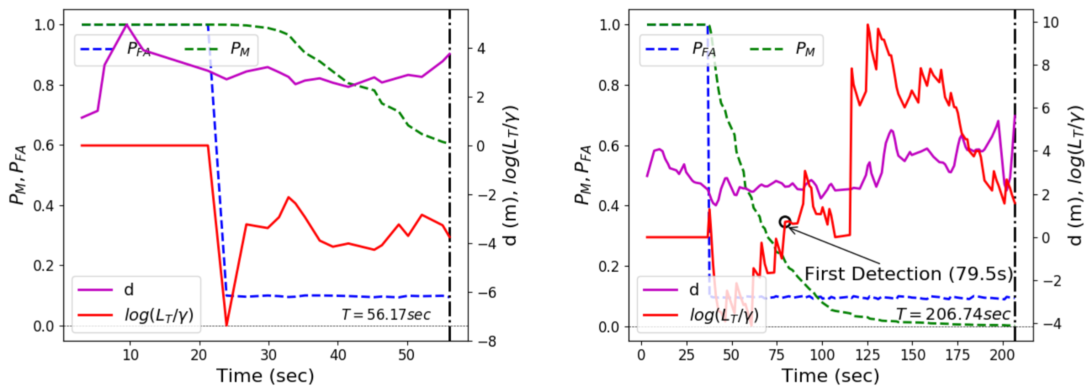

(a) GM-90 Indoor Run

(b) GM-90 Outdoor Run

Fig. 6: Detection parameters for the autonomous airborne GM-90 counter as a function of decision time T. Bound on probability of false alarm: dashed blue; bound on the probability of missed detection: dashed green; ratio $\log {}^{L_T}/_{\gamma}$: solid red; sensor-source distance: solid magenta. (a) Detection time interval 56 seconds.(b) Detection time interval 206 seconds.

the probability of missed detection is still around 0.6, thus comparable to the conditions under which the detection of Fig. 5 was achieved, but this value for T is below the 5% percentile for the recommended exposure time.

Figure 6(b) depicts the results of a longer chase by the MAV carrying the GM-90 counter conducted outdoors. This time, the integration window was extended to more than 200 seconds. In addition to the effect of sensor integration window length on detection accuracy, Fig. 6(b) shows more clearly the evolution of the bounds on the decision test's error probabilities P_{FA} and P_{M}. At the time of decision, the bound on the probability of miss, P_{M} is almost zero, indicating very high probability for accurate decision-making. Although the statistic $\log {}^{L_T}/_{\gamma}$ crosses zero and becomes positive for the first time shortly after 70 seconds, at that time the bound on P_{M} is still over 0.3, which is relatively high (one-in-three chance of missing a source). After 120 seconds, however, the statistic $\log {}^{L_T}/_{\gamma}$ stays steadily above the threshold of 0, indicating a confident decision. It is of note that towards the end of the integration window, the statistic $\log {}^{L_T}/_{\gamma}$ decreases, most likely due to the target being able to open up its distance with respect to the pursuing MAV—which by that time was experiencing a drop in its power reserves; same trend can be noticed in Fig. 6(a).

VI. Comparison with Alternative Methods

This section provides a qualitative comparison with methodologies available in the literature for the detection of mobile radiological signatures. It needs to be noted that such comparisons can only be performed at a qualitative level because the experimental setup and structure is significantly different between what is presented in this paper and what has been reported in literature. Among the fundamental differences, besides the fact that typically sources utilized were strong, is that sensor mobility has not been used explicitly for the purpose of facilitating the detection of a fleeting source, or that the hardware utilized was quite sophisticated and expensive. Specifically, on one side one can find existing approaches to detecting a moving source that rely on measurements from a *static* (i.e., stationary) sensor network, and on the other there exists very interesting work that deploys heavy-duty UAVs with *high-end* scintillators. In contrast, the work reported in this paper aims in the middle of this range, motivated by the need to be able to deploy highly-agile autonomous mobile networked sensors *economically* and *at scale*.

With these caveats, one conceptually comparable approach utilizes a static network of three COTS sensors in an effort to detect a moving source [12]. The data (acquired as a log-likelihood of radiation intensity) from the sensors have been fused in a sequential manner and compared against a pre-selected threshold. A near zero false alarm rate is shown to be achievable with an integration window of approximately 120 seconds. Although detection is quick and with a low false alarm rate, the source is kept very close to the sensors (within a distance of 1–20 cm) and its activity is an order of magnitude stronger than the one considered in this paper.

Another existing approach draws from Domestic Nuclear Detection Office (DNDO)'s Intelligent Radiation Sensing System (IRSS) indoor and outdoor datasets [15] that typically feature a static network of 16–18 NaI 2 in $\times$2 in scintillators in either a 40 ft$\times$40 ft indoor or 50 m $\times$ 50 m outdoor space where a (static) sensor network is deployed. Data from Cs-137 sources of intensity varying between 7.2-350 μCi are fused [21] as part of a methodology that also aims at spatially localizing them. In one such experiment, a moving source was localized in about 100 seconds. The detection time is comparable to the one reported in this work, with the difference being that in the former, data from *many* (static) sensors are utilized. In an approach that *does* leverage sensor mobility [7], a 4 kg sensor payload package (CLLBC scintillators + LiDAR) is fitted on a DGI600 Matrice; a ^{60}Co gamma source of intensity 500μCi, and a mixed (^{252}Cf, ^{133}Ba, ^{137}Cs) Pu surrogate neutron source of approximate intensity 300 μ Ci have been utilized as targets, but detection times are not reported. Another example of sensor mobility [7] involves a 2 in $\times$ 4 in$\times$ 16 in NaI(Tl) scintillator mounted on a car for the purpose of detecting a

189 μCi ^{137}Cs source.

Even when detection times are comparable, the aforementioned examples employ setups that differ from the one reported here in one (or more) different aspects:

- significantly stronger sources were deployed;
- higher-end (i.e., more expensive) detectors are utilized;
- multiple sensor (vs single) data streams were fused;
- the sensor platform was heavier and more expensive;
- the sensor payload was heavier and more sophisticated.

Having said that, it should also be acknowledged that the existing literature presents methodologies to infer additional characteristics, such as source intensity, localization, speed, etc. Some of these features can possibly be utilized in the reported sensor system in future realizations; at this time, the target ground platform that may be a carrier of a radiological signature is assumed to be known.

VII. Conclusions

This paper reports on the development of an autonomous aerial radiation detector which can leverage its mobility to achieve significant improvements in detection performance (in terms of time or distance) for weak radioactive sources in transit compared to current alternatives. Given that the experimental setup and structure of the problems reported in the literature is notably different from the one examined here, it is difficult to draw a quantitative comparison to determine exactly how much better the reported system performs. Yet, in addition to performance improvements, the reported system contributes to democratization of radiation detection platforms, making it possible to deploy small MAVs carrying low-cost, COTS sensors for detecting weak radiological signatures, as opposed to utilizing high-end infrasture or using the sensors only in controlled laboratory experiments. With this new sensor modality a source of less than 10 μCi intensity, moving at speeds of 1–2 m/s, can be detected in about $1^1/_2$ minutes. The sensor design described lowers the cost barrier to scalability to networks of mobile sensors, as well as the incorporation of more advanced (networked) information fusion and decision-making algorithms [25].

References

[1] FlyCam UAV. https://www.flycamuav.com/aerial-radiation-detection/.

[2] R.C. Byrd, J.M. Moss, W.C. Priedhorsky, C.A. Pura, G. W. Richter, K.J. Saeger, W.R. Scarlett, S.C. Scott, and R.L. Wagner Jr. Nuclear detection to prevent or defeat clandestine nuclear attack. *IEEE Sensors Journal*, 5(4):593–609, 2005.

[3] Andrea Chierici, Andrea Malizia, Daniele di Giovanni, Francesca Fumian, Luca Martellucci, Pasquale Gaudio, and Francesco d'Errico. A low-cost radiation detection system to monitor radioactive environments by unmanned vehicles. *The European Physical Journal Plus*, 136, 2021.

[4] R. A. Cortez, H. G. Tanner, R. Lumia, and C. T. Abdallah. Information surfing for radiation map building. *International Journal of Robotics and Automation*, 26(1):4–12, 2011.

[5] Tairan Liu, Angela Di Fulvio, Long Kiu Chung, and Kimberlee J Kearfott. Radiation mapping for an unmanned aerial vehicle: Development and simulated testing of algorithms for source mapping and navigation path generation. *Health Physics*, 120(3):321–338, March 2021.

[6] C. Y. T. Ma, D. K. Y. Yau, N. K. Yip, N. S. V. Rao, and J. Chen. Performance analysis of stochastic network coverage with limited mobility. In *Proceedings of 6th IEEE International Conference on Mobile Adhoc and Sensor Systems*, pages 496–505, Oct 2009.

[7] M. R. Marshall, D. Hellfeld, T. H. Y. Joshi, M. Salathe, M. S. Bandstra, K. J. Bilton, R. J. Cooper, J. C. Curtis, V. Negut, A. J. Shurley, and K. Vetter. 3-d object tracking in panoramic video and lidar for radiological source–object attribution and improved source detection. *IEEE Transactions on Nuclear Science*, 68(2):189–202, 2021.

[8] Robert J. Nemzek, Jared S. Dreicer, David C. Torney, and Tony T. Warnock. Distributed sensor networks for detection of mobile radioactive sources. *IEEE Transactions on Nuclear Science*, 51(4):1693–1700, 2004.

[9] Chetan D. Pahlajani, Jianxin Sun, Ioannis Poulakakis, and Herbert G. Tanner. Error probability bounds for nuclear detection: Improving accuracy through controlled mobility. *Automatica*, 50(10):2470–2481, 2014.

[10] Raghu Pasupathy. Generating nonhomogeneous Poisson processes. In *Wiley Encyclopedia of Operations Research and Management Science*. Wiley, 2009.

[11] R. Pavlovsky, J. Cates, W. J. Vanderlip, T. Joshi, A. Haefner, E. Suzuki, R. Barnowski, V. Negut, A. Moran, K. Vetter, and B. Quiter. 3d gamma-ray and neutron mapping in real-time with the localization and mapping platform from unmanned aerial systems and man-portable configurations. *arXiv: Instrumentation and Detectors*, 2019.

[12] Lijun Qian, John Fuller, and Ing Chang. Quickest detection of nuclear radiation using a sensor network. In *Proceedings of IEEE Conference on Technologies for Homeland Security*, pages 648–653, 2012.

[13] N. S. V. Rao, C. W. Glover, M. Shankar, Y. Yang, J. C. Chin, D. K. Y. Yau, C. Y. T. Ma, and S. Sahni. Improved SPRT detection using localization with application to radiation sources. In *12th International Conference on Information Fusion*, pages 633–640, July 2009.

[14] N. S. V. Rao, M. Shankar, J. C. Chin, D. K. Y. Yau, C. Y. T. Ma, Y. Yang, J. C. Hou, X. Xu, and S. Sahni. Localization under random measurements with application to radiation sources. In *Proceedings of 11th International Conference on Information Fusion*, pages 1–8, June 2008.

[15] Nageswara Rao, Satyabrata Sen, Chase Wu, Mark Berry, Kayla Grieme, R. Brooks, and Guthrie Cordone. Datasets for radiation network algorithm development and testing. In *Proceedings of IEEE Nuclear Science Symposium and Medical Imaging Conference*, November 2016.

[16] B. Ristic, A. Gunatilaka, and M. Rutten. An information gain driven search for a radioactive point source. In *Proceedings of 10th International Conference on Information Fusion*, pages 1–8, July 2007.

[17] Donald L. Snyder. *Random point processes*. Wiley New York, 1975.

[18] Devabhaktuni Srikrishna, A. Narasimha Chari, and Thomas Tisch. Deterance of nuclear terrorism with mobile radiation detectors. *The Nonproliferation Review*, 12(3):573–614, 2005.

[19] Jianxin Sun and Herbert G. Tanner. Constrained decision making for low-count radiation detection by mobile sensors. *Autonomous Robots*, 39(4):519–536, 2015.

[20] H. L. Van Trees, K. L. Bell, and Z. Tian. *Detection Estimation and Modulation Theory, Part I: Detection, Estimation, and Filtering Theory*. Wiley, 2013.

[21] Chase Qishi Wu, Mark Lee Berry, Kayla Marie Grieme, Satyabrata Sen, Nageswara S.V. Rao, Richard R. Brooks, and Guthrie Cordone. Network detection of radiation sources using localization-based approaches. *IEEE Transactions on Industrial Informatics*, 15(4):2308–2320, 2019.

[22] I. Yadav and H. G. Tanner. Controlled mobile radiation detection under stochastic uncertainty. *IEEE Control Systems Letters*, 1(1):194–199, July 2017.

[23] I. Yadav and H. G. Tanner. Reactive receding horizon planning and control for quadrotors with limited on-board sensing. In *Proceedings of IEEE/RSJ International Conference on Intelligent Robots and Systems*, pages 7058–7063, 2020.

[24] Indrajeet Yadav, Kevin Eckenhoff, Guoquan Huang, and Herbert G. Tanner. Motion planning and visual-inertial target tracking for uav-based radiation detection. In *Proceedings of 28th Mediterranean Conference on Control and Automation*, pages 1009–1014, 2020.

[25] Indrajeet Yadav, Chetan D. Pahlajani, Herbert G. Tanner, and Ioannis Poulakakis. Information-sharing and decision-making in networks of radiation detectors. *Autonomous Robots*, 42(8):1715–1730, Dec 2018.